Appl. Phys. B 92, 367–378 (2008)
DOI: 10.1007/s00340-008-3132-1

Applied Physics B
Lasers and Optics

C.F. KAMINSKI[1,2]
R.S. WATT[1]
A.D. ELDER[1]
J.H. FRANK[3]
J. HULT[1,✉]

Supercontinuum radiation for applications in chemical sensing and microscopy

[1] Department of Chemical Engineering, University of Cambridge, Pembroke Street, Cambridge CB2 3RA, UK
[2] SAOT School of Advanced Optical Technologies, Max-Planck Research Group, University of Erlangen-Nürnberg, 91058 Erlangen, Germany
[3] Combustion Research Facility, Sandia National Laboratories, Livermore, CA, USA

Received: 27 February 2008/Revised version: 11 June 2008

ABSTRACT The advent of compact, high brightness supercontinuum radiation sources employing solid core photonic crystal fibres is beginning to make an impact across the field of applied spectroscopy research. In this article we focus on the use of supercontinuum sources to construct novel instrumentation for chemical sensing. A brief overview is given on the mechanisms of supercontinuum generation in solid core photonic crystal fibres, and then we review recent, and present new, results from our own research. We present examples on gas phase sensing applications, permitting wide bandwidth molecular spectra to be gathered at ultrahigh speed. Furthermore we demonstrate the design and construction of a wide bandwidth microscope for wavelength flexible hyperspectral confocal imaging. We conclude with an outlook and a summary of where and how we think the field may develop over coming years.

PACS 07.07.Df; 42.62.Fi; 87.64.mk; 87.64.-t

1 Introduction

Optical sensing technology is undergoing a revolution with major technological advances having emerged over recent years that are set to change the way in which we probe the physics and chemistry in a huge range of scientific processes. One of the most exciting new technologies to emerge from the photonics research community is the possibility to generate broad bandwidth, spatially coherent radiation of extreme spectral brightness [1]. This so-called supercontinuum radiation is generated through non-linear processes upon intense pumping of optical materials. The effect can be massively enhanced in holey fibre structures, so-called photonic crystal fibres (PCFs) [2, 3], and as a result supercontinuum (SC) radiation can be generated routinely and relatively inexpensively; SC sources are beginning to replace a range of traditional light sources in an ever increasing number of laboratories around the world. Novel science has emerged through supercontinuum generation, most notably in the field of optical frequency metrology through the concept of optical frequency combs [4]. SC sources have also found applications for pulse compression [5], telecommunication [6], semiconductor and optical component characterisation [7–10], atmospheric analysis and remote sensing [11], spectroscopic gas sensing [12–14], non-linear spectroscopy [15], optical coherence tomography [16], confocal microscopy [17–19], etc. In the present paper we focus on the use of supercontinua generated in solid core PCF structures in the context of chemical sensing, with applications ranging from gas phase sensing to spectroscopy applications in microscopic systems. The paper focuses on some very recent, and also new, results obtained in our group to illustrate the power of supercontinuum-based chemical sensing. Some of this research was presented at the most recent FLAIR (Field Laser Applications in Industry and Research) conference that took place in Florence between the 2nd and 7th of September, 2007.

The paper begins with a brief outline on the physics of supercontinuum generation, which is illustrated using numerical simulations of the SC generation process. This is followed by a short overview of supercontinuum technology, and finally examples are presented on practical applications. In the first example, an ultrarapid gas phase sensing absorption spectrometer is presented, capable of acquiring spectra over hundreds of nanometer bandwidth at over 100 kHz repetition rate. In the second example the technology is used to demonstrate the use of SC technology for spectral scanning imaging microscopy, permitting chemical signatures to be measured at microscopic resolution with high specificity. Overall the paper demonstrates that a supercontinuum comes close to being the ideal source for the chemical analyst: The huge bandwidth gives high specificity and flexibility, as a large number of spectroscopic transitions can be covered and many species can be detected simultaneously. The high spectral brightness and spatial coherence permit energy to be deployed where it is needed, crucial for sensing at a distance, or for probing at high spectral resolution. The spatial coherence also makes it easy to use SC sources in microscopy applications. The short pulse nature of supercontinua yields excellent time resolution; picosecond or even femtosecond pulse widths are routinely achievable. Finally, SC sources are becoming ever more compact and rugged, containing few if any optical or mechanical components. At the same time their operating range is being pushed ever deeper into the UV on the one hand and into the IR on the other. The time is set for SC radiation to be deployed in the field in a huge range of applications.

✉ Fax: +44-1223-334796, E-mail: jfh36@cam.ac.uk

2 Supercontinuum generation

SC radiation is generated by focusing intense laser pulses into solid, fluid or gaseous media, where a variety of non-linear optical processes such as self-phase modulation, cross-phase modulation, self-steepening, four-wave mixing, and stimulated Raman scattering [1, 20] act to dramatically broaden the spectrum. Of particular interest to practical applications is the high efficiency of supercontinuum generation in solid core photonic crystal fibres (PCFs) [2, 3]. The dispersion characteristics and small core diameter of such fibres enhance the non-linear processes, and permit broadband supercontinua to be generated at pump pulse energies in the sub-nJ range with femtosecond lasers. It is instructive to study the physical processes responsible for the spectral broadening of an optical pulse into a supercontinuum in such a fibre. In order to do this we present here results from numerical simulations performed in our group and we compare the SC generation process resulting from both femtosecond and picosecond pumping. The process of SC generation is now well understood and the tutorial discussion in this section follows closely along the lines of that in references [3, 20, 21], but we provide it here for the sake of completeness and so that this article provides a self-contained discussion of this area.

The generalised non-linear Schrödinger equation (GNLSE), which can be derived from analytic simplifications of Maxwell's equations, accurately describes the process of supercontinuum generation [20]. The GNLSE is a non-linear partial differential equation that, in almost all cases, cannot be solved analytically; a numerical approach is therefore necessary. Numerical modelling of supercontinuum generation permits one to explore the underlying spectral broadening processes [3, 21]. The GNLSE describes the evolution of the complex field envelope of the optical pulse $A(z,t)$:

$$\frac{\partial A}{\partial z} = -\frac{\alpha}{2}A - \sum_{k\geq 2}\beta_n \frac{i^{n-1}}{n!}\frac{\partial^n A}{\partial T^n} + \mathrm{i}\gamma\left(1+\frac{1}{\omega_0}\frac{\partial}{\partial T}\right) \times \left(A(z,T)\int_0^\infty R(T')\left|A(z,T-T')\right|^2 \mathrm{d}T'\right), \qquad (1)$$

where z is the distance, T is the retarded time travelling at the envelope group velocity, and the field envelope $A(z,t)$ is normalized such that the instantaneous power is given by $|A(z,t)|^2$. The first term on the right hand side models fibre losses, where α is the attenuation constant. Dispersion is modelled by the second term, where β_n are the higher order dispersion coefficients obtained by a Taylor series expansion of the propagation constant $\beta(\omega) = n(\omega)\omega/c$ around the centre frequency ω_0. The last term models non-linear effects, the intensities of which are determined by the non-linear coefficient γ. The non-linear response function $R(T) = (1-f_\mathrm{R})\delta(T) + f_\mathrm{R}h_\mathrm{R}(T)$ includes both the instantaneous electronic and the delayed Raman contributions to the non-linear polarisation. The fractional contribution of the delayed Raman response is represented by f_R, for which a value of $f_\mathrm{R} = 0.18$ is often assumed for silica [22]. For the Raman response function of a silica fibre, $h_\mathrm{R}(t)$, the experimentally determined cross-section [22], or an analytical representation of the same can be used [23, 24]. The temporal derivative in the non-linear term is responsible for higher order non-linear effects, such as pulse self-steepening and optical shock formation.

The most commonly employed numerical scheme for solving (1) is the split-step Fourier method [20]. In the split-step method, dispersive and non-linear effects are separately integrated, and the results are combined to construct the full solution after each step through the fibre. The dispersive term, which is linear, is evaluated in the frequency domain through the use of the fast Fourier transform (FFT), whereas the non-linear term is treated in the time domain. The split-step method is normally combined with a Runge–Kutta method for integration of the non-linear step. Here, however, a fourth-order Runge-Kutta in the interaction picture method with adaptive step sizing has been employed for solving (1) [25].

Both the examples described here correspond to pumping of a PCF with a zero dispersion wavelength of 1046 nm with laser pulses centred around 1065 nm, in the so-called anomalous dispersion regime of the fibre. The fibre parameters used for the simulations are: $\gamma = 0.011\,\mathrm{W}^{-1}\,\mathrm{m}^{-1}$, $\beta_2 = -2.56\,\mathrm{ps}^2/\mathrm{km}$, $\beta_3 = 8.01\times 10^{-2}\,\mathrm{ps}^3/\mathrm{km}$, $\beta_3 = -1.35 \times 10^{-3}\,\mathrm{ps}^4/\mathrm{km}$, $\beta_5 = 4.01\times 10^{-7}\,\mathrm{ps}^5/\mathrm{km}$, and $\beta_6 = -7.25 \times 10^{-10}\,\mathrm{ps}^6/\mathrm{km}$, which correspond to a type of PCF commonly employed for SC generation in this spectral region [10]. Supercontinuum generation under similar conditions has previously been explored numerically by Genty et al. [21]. For the simulations presented here the analytical form of $h_\mathrm{R}(t)$, proposed by Hollenbeck and Cantrell [24], was used. Quantum-limited shot noise on the injected input field was included to correctly reproduce the evolution of the spectral broadening, which is important in particular for longer pulses [3].

For the first example, the initial pulse that is used in the simulations has a hyperbolic secant profile $A(0,T) = \mathrm{sqrt}(P_0)\mathrm{sech}(T/T_0)$, where the peak power P_0 is 10 kW, and the width T_0 is 28.4 fs, which corresponds to an intensity FWHM of 50 fs. In Fig. 1 the evolution of the (a) spectral and (b) temporal intensity profile of the pulse is shown as it propagates through a 15 cm long fibre. The evolution of the pulse is plotted as intensity density plots, on a logarithmic scale which has been truncated at −25 dB relative to the peak value. Spectral broadening is seen to take place already over the first three centimetres of the fibre. This initial broadening, which is caused by the interaction between self-phase modulation and dispersion, is symmetric. After this initial stage the spectrum quickly becomes asymmetric, and distinct spectral peaks develop on both sides of the pump wavelength due to a process known as soliton fission. For the input pulse the soliton order is $N \approx 5.9$ under those conditions. Higher order dispersive and non-linear perturbations cause the fission of the higher order soliton into multiple fundamental solitons, and this process is seen to be initiated at a distance of around 3.5 cm. The resulting fundamental solitons then undergo a continuous self-frequency shift to longer wavelengths because of intrapulse Raman scattering. The emergence and self-shifting of one of the most intense of these fundamental solitons on the long wavelength side is clearly seen in Fig. 1a. In this process, each Raman soliton sheds some of its energy in the form of a dispersive wave on the short wavelength side

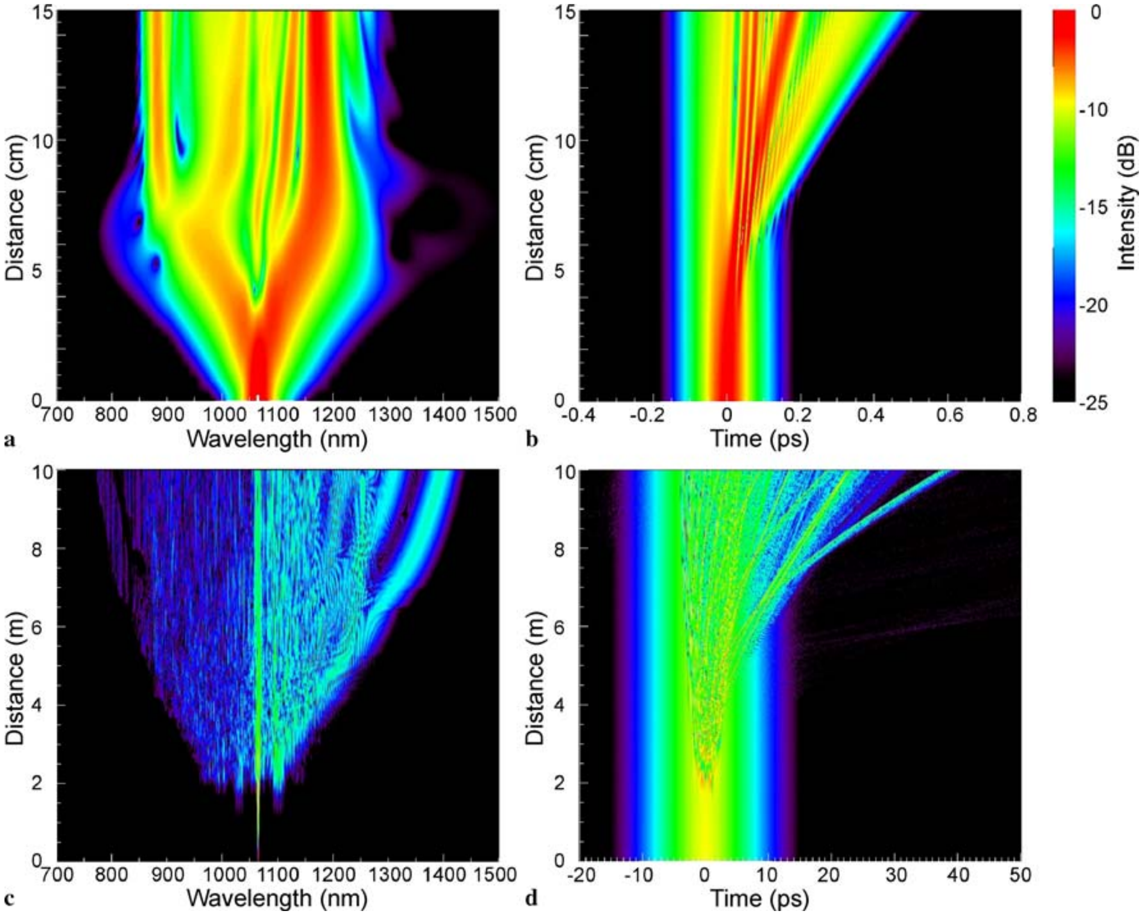

FIGURE 1 Results from numerical simulations of supercontinuum generation in a PCF when pumping with a 1065 nm pulse. (**a**) The spectral and (**b**) temporal evolution as a function of the propagation distance are shown as (logarithmic) intensity density plots for an input pulse with a temporal width of 50 fs FWHM. (**c**) Spectral and (**d**) temporal evolution for an input pulse with a temporal width of 5 ps FWHM

of the pump, which leads to the appearance of discrete spectral components also in this region of the spectrum. The appearance of fundamental solitons and their associated dispersive waves are also observed in the time domain, Fig. 1b, where they are seen to separate from the main pulse due to the reduction in group velocity caused by their spectral shifts. Higher order dispersion eventually limits the soliton self-frequency shift, and after 8 cm the most intense soliton ceases to shift to higher wavelengths. Effects such as cross-phase modulation and four-wave mixing can also act to further broaden the spectrum. The type of dynamics observed here is typical of supercontinua generated using ultrashort pulses in the anomalous dispersion regime of highly non-linear fibres [3, 20, 21].

The second example corresponds to a pulse with a peak power P_0 of 500 W and an intensity FWHM of 5 ps being injected into a 10 m long fibre. The resulting spectral and temporal intensity density plots are shown in Fig. 1c and d, respectively. The spectral evolution of the picosecond generated SC clearly appears quite different compared to the femtosecond case above. The main reason for this difference is that the processes of four-wave mixing and Raman scattering dominate the initial generation of the SC for picosecond or nanosecond pulses. For such pulses self-phase modulation induced broadening is inefficient, and instead the first spectral broadening observed, after 1.5 m in Fig. 1c, is an isolated sideband structure centred around the pump, at 1030 and 1100 nm. This pair of sidebands corresponds to the downshifted Stokes and upshifted anti-Stokes bands of a phase-matched degenerate four-wave mixing process which grows from noise. In the time domain (Fig. 1d) this process leads to the development of an ultrafast intensity modulation instability, which is clearly seen at the peak of the pulse after about 2 m. Further sideband generation and stimulated Raman scattering then further broadens the spectrum and also act to merge the spectral features. After about 5 m we see distinct soliton structures appearing and contributions from soliton Raman self-frequency shifting, cross-phase modulation and dispersive wave generation then results in a further increase in the SC spectral width, predominantly to longer wavelengths. As the SC generation process for longer pulses is initiated by growth from noise, the temporal coherence of the resulting SC is generally much lower than that of a SC generated by femtosecond pumping [3]. The same is also true for the intensity stability, where significant shot-to-shot fluctuations in the spectral envelope are observed for longer pump pulses [21].

3 Supercontinuum sources

For the generation of broadband supercontinuum radiation a suitable combination of a pump laser and a fibre is needed. A wide variety of laser types, with pulse lengths ranging from femtoseconds to nanoseconds, and even continuous wave, have been employed for SC generation. With femtosecond pump pulses it is possible to generate broadband SC in highly non-linear PCFs even with pulse energies lower than 1 nJ [2]. Common sources of femtosecond pulses employed for this purpose include mode-locked Ti:sapphire lasers [2, 26], erbium-doped fibre lasers [13, 27, 28], and chromium-doped forsterite ring lasers [29], which all operate at repetition rates of 10 s or 100 s of MHz. The spectral power density of femtosecond pumped SC are limited by the pump laser output powers and by fibre damage thresholds to around 100 µW/nm. To achieve higher spectral densities it is thus advantageous to employ longer pump pulses. With picosecond pumping spectral power densities of mW/nm are possible [30, 31]. Mode-locked ytterbium or erbium fibre lasers, emitting pulses a couple of picoseconds long and operating at repetition rates of 10 s of MHz are often employed for this purpose [14, 31, 32]. The simplest and most inexpensive pump sources for achieving broadband SC radiation, however, are Q-switched Nd:YAG microchip lasers [31, 33]. Those microchip lasers typically feature pulse lengths around 1 ns and repetition rates in the kHz range. The spectral power density of the resulting SC are similar to those achieved using femtosecond pumping. It is also worth noting that SC generation using continuous wave fibre lasers for pumping is possible [27], with output powers as high as 29 W recently demonstrated [34].

The type of fibre that has really revolutionised supercontinuum generation is the photonic crystal fibre (PCF) [2, 26, 30, 33, 35]. The type of PCF used for SC generation has a solid silica core, surrounded by an array of micrometer sized air holes running along its length. In such a fibre the effective refractive index of the surrounding air hole region is lower than that of the solid core, and thus light is guided in a similar fashion to conventional fibres. By varying the hole size and periodicity the fibre waveguide properties can be engineered in ways that are not possible in conventional fibres [36]. Of particular importance for SC applications are the possibilities of simultaneously tailoring the group velocity dispersion characteristics and tightly confining the light, which enhances non-linearity. As a result SC can be generated much more efficiently than in conventional fibre. Short wavelength SC radiation is attractive for many spectroscopic applications. By tapering a PCF, the zero dispersion wavelength can be made to continuously decrease along the fibre, which allows the SC to be extended towards shorter wavelengths. In this way SC spectra extending down to 372 nm have been generated [31]. The same effect can also be achieved by splicing multiple PCFs in series [37].

One of the alternatives to the PCF is the highly non-linear fibre (HNLF), where an increased non-linear coefficient is obtained for example by doping with germanium [27, 29]. The first example of SC generation in fibres, however, was performed in conventional fibres [38]. Standard single-mode fibres exhibit a higher optical damage threshold than narrow-core PCFs, and are thus still attractive for applications requiring high pulse energy SC and have successfully been employed for generation of high pulse energy (µJ) supercontinuum pulses in the visible [38, 39] and near-infrared (IR) spectral regions [14, 32, 39, 40]. Supercontinuum generation in single-mode fibres has recently also been demonstrated in the UV spectral region [41] and by using ZBLAN fibres also in the mid-IR [42, 43] spectral region.

In the last couple of years commercial SC sources, based on mode-locked fibre lasers or Q-switched microchip lasers combined with suitable PCFs, have been developed. Today such systems offer broadband spectral coverage over the visible and near-IR spectral regions with multi-Watt output powers, in compact turnkey units.

4 Applications for gas sensing

Supercontinuum sources are well suited for gas sensing, as they provide broadband spectral coverage in the near-IR region, where many gaseous species of interest for chemical processes or atmospheric sensing applications have vibrational overtone transitions. The simplest implementation of an absorption measurement based on a SC source is a direct absorption measurement employing a spectrometer for detection. In this configuration the high repetition rate light source can be regarded as a quasi-continuous wave source. The spectrometer used for detection would ideally feature both high spectral resolution, to allow unambiguous identification of spectral lines, and broad wavelength coverage to allow entire spectral bands of one or more species to be recorded. Here the study of one of the ro-vibrational overtone bands of H_2O, stretching from 1350 to 1500 nm, will serve as an example of the broadband capability of SC-based sensors [14]. Spectra encompassing entire ro-vibrational bands of C_2H_2 [14, 44, 45], CH_4 [46], and C_2H_4 [14] have also been measured in a similar manner.

The experimental set-up employed for absorption measurements in gaseous samples is illustrated in Fig. 2a. Here

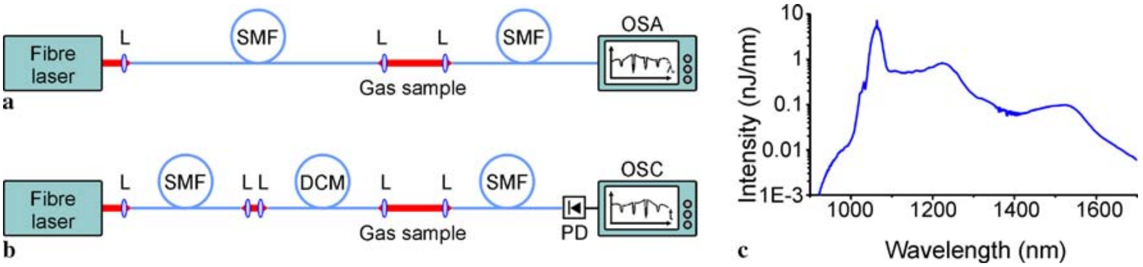

FIGURE 2 Experimental set-up for (**a**) conventional, and (**b**) time-resolved supercontinuum-based absorption measurements (L lens, SMF single mode fibre, DCM dispersion compensating module, PD photo-diode, OSC oscilloscope, OSA optical spectrum analyzer). (**c**) Spectral profile of the supercontinuum radiation generated in the single-mode fibre

supercontinuum radiation was generated in a conventional single-mode fibre (Corning, SMF28), where efficient spectral broadening to higher wavelengths can be achieved by pumping with μJ pulse energies [14, 32]. The pump laser (Fianium, FemtoPower 1060) was a passively mode-locked ytterbium fibre laser emitting 5 ps long pulses with a centre wavelength of 1064 nm. An acousto-optic pulse picker allowed the repetition rate to be varied between 0.3 and 20 MHz. The output pulse energy increases from 45 nJ at 20 MHz repetition rate to over 1.4 μJ at 0.3 MHz repetition rate. The spectral profile of the supercontinuum radiation, shown in Fig. 2c, covers the 1300 to 1700 nm spectral region, which is of particular interest for the detection of small molecules. The supercontinuum radiation exiting the fibre is collimated, passed through the measurement region, and finally launched back into a SMF28 fibre. All fibres employed are single mode in the spectral range used for the absorption measurements. The spectral profile of the transmitted radiation is then recorded on an optical spectrum analyser (OSA). The OSA (Yokogawa, AQ6317C) was operating at a resolution of around 15 pm.

For the H_2O absorption measurements reported here the collimated SC beam was passed through approximately 2.8 m of air (39% relative humidity, 24 °C). The transmitted intensity is shown in Fig. 3a. The spectral region shown stretches from 1340 to 1500 nm, and covers the entire ro-vibrational structure of the H_2O band which consists of more than 400 individual absorption features. In Fig. 3b the corresponding absorption spectrum is shown, which was obtained by fitting a baseline to the transmission trace. The H_2O linewidth is about 33 pm at ambient conditions, which means that the observed spectral lines are slightly under-resolved. A calculated spectrum corresponding to the experimental conditions and based on line strength and lineshape data from the HiTran 2004 database [47] is shown in Fig. 3c. To allow a direct comparison between the experimental and the HiTran spectrum, the latter has been convolved with a Gaussian filter with a width of 15 pm, corresponding to the experimental resolution. Overall, the two spectra are seen to agree very well, which is further evident from the magnified view shown in Fig. 3d.

Employing a grating spectrometer, such as an OSA, for detection is time consuming and thus only useful for studying stationary samples. However, acquisition times can be shortened by several orders of magnitudes by employing time-of-flight measurement techniques. Temporally resolved measurements are achieved by transforming the broadband SC pulses into rapid wavelength sweeps by employing a suitable dispersive element, such as a fibre [48] or an atomic vapour [49], where the different spectral components of the pulse propagate at different speed. The detection of the light transmitted through the sample is then performed in the temporal domain. The high repetition rate of SC sources allows for the acquisition of broadband spectra at rates exceeding 100 kHz [46], which makes probing of transient and non-stationary flows possible. This technique is demonstrated here by acquiring spectra of the $2\nu_3$ band in CH_4 [46]. In the same fashion absorption spectra have been acquired in the time domain of gaseous C_2H_2 [12, 13, 44], CO_2 [13], C_2H_6O [13], H_2O [13, 14], and CO [50].

For the rapid acquisition of CH_4 spectra the experimental set-up shown in Fig. 2b was used. The broadband supercontinuum pulses were launched into a dispersive fibre where a rapid wavelength sweep was created, as different spectral components of the pulse travel through the fibre at different group velocities. The fibre employed for this purpose was a dispersion compensating module (DCM), featuring large negative dispersion (Fujikura, G652-C+L-band SC-DCFM). The wavelength dependence of the dispersion was measured using a time-of-flight technique [10]. The absolute value of the dispersion increases from 0.9 ns/nm at 1300 nm to 2.2 ns/nm at 1650 nm, which causes the output from the DCM to sweep from 1300 to 1700 nm in approximately 600 ns. For the experiments reported here a repetition rate of 1.133 MHz was employed, which is the highest repetition rate at which the generated dispersed supercontinuum sweeps remain temporally separated. For the absorption measurements presented here the SC radiation was passed through a 105 mm long path of CH_4 mixed with air ($\sim 20\%$ CH_4). The transmitted beam was then launched back into a single-mode fibre and its intensity detected by a 10 GHz bandwidth preamplified photodiode (Terahertz Technologies, TIA-3000). The photodiode output was finally digitized using an 8 GHz bandwidth real-time oscilloscope (Tektronix, TDS6804B, 20 GS/s), making it possible to observe and store a large number of individual wavelength sweeps. Under the condition that the laser pulse width is shorter than the time response of the detection system, $\Delta\tau$, the spectral resolution of this type of measurement is given by $\Delta\lambda = \Delta\tau/D$, where D is the dispersion of the fibre [13]. One option to improve spectral resolution is thus to increase the dispersion, which is normally associated with increased optical losses. The other option is to decrease the time response of the detection system, however, it is important to notice that the resolution possible to achieve in this manner will ultimately be uncertainty-limited, as the short temporal detection window employed limits the width of the instantaneous wavelength [13, 51].

Figure 4a shows the intensity profile of the transmitted SC sweep as a function of arrival time at the detector. The instantaneous wavelength, which was determined using the DCM dispersion curve [10], is indicated at the top of the figure. Due to the negative dispersion of the DCM the longest wavelengths arrive first at the detector. The 600 nm wide spectrum is scanned in only 800 ns. Two sets of absorption lines are clearly seen in the transmission trace. The first group of peaks, extending from 1620 to 1700 nm, corresponds to the P-, Q-, and R-branches of the $2\nu_3$ vibrational overtone transition in CH_4. The second group of peaks, extending from 1350 to 1420 nm corresponds to overtone transitions in H_2O, present in the air. The trace shown in Fig. 4a corresponds to an average of 1000 wavelength sweeps, for which the total acquisition time was around 0.9 ms. The fluctuations in the supercontinuum spectral profile from shot-to-shot are quite large, as indicated by the error bars, which correspond to the standard deviation of individual spectra at three different spectral positions around the CH_4 absorption band. At the centre of the CH_4 transition the relative standard deviation is more than 50%. The CH_4 absorbance, shown in Fig. 4b, was calculated from the transmitted radiation by fitting a baseline to the transmitted intensity profile. For this averaged spectrum the observed signal-to-noise ratio was around 190 for the strongest peak in the R-branch, which is relatively good considering that an 80 nm wide spectrum, covering almost the entire *P*-, *Q*-, and *R*-branches, was recorded in less than a millisecond. The spectral resolution of the dispersed supercontinuum absorption measurement is around 39 pm in this spectral region, as determined by the dispersion of the DCM (2.2 ns/nm) at this wavelength and the measured time response of the detection system (85 ps) [46], which is close to the actual width (38 pm at ambient conditions) of the CH_4 lines. A calculated spectrum, corresponding to the same conditions as in the experiment is shown in Fig. 4c. Line strength and line shape data were taken from the HiTran 2004 database [47]. The HiTran spectrum has been convolved with a Gaussian filter, the width of which (FWHM = 39 pm) corresponds to the experimentally determined spectral resolution of the absorp-

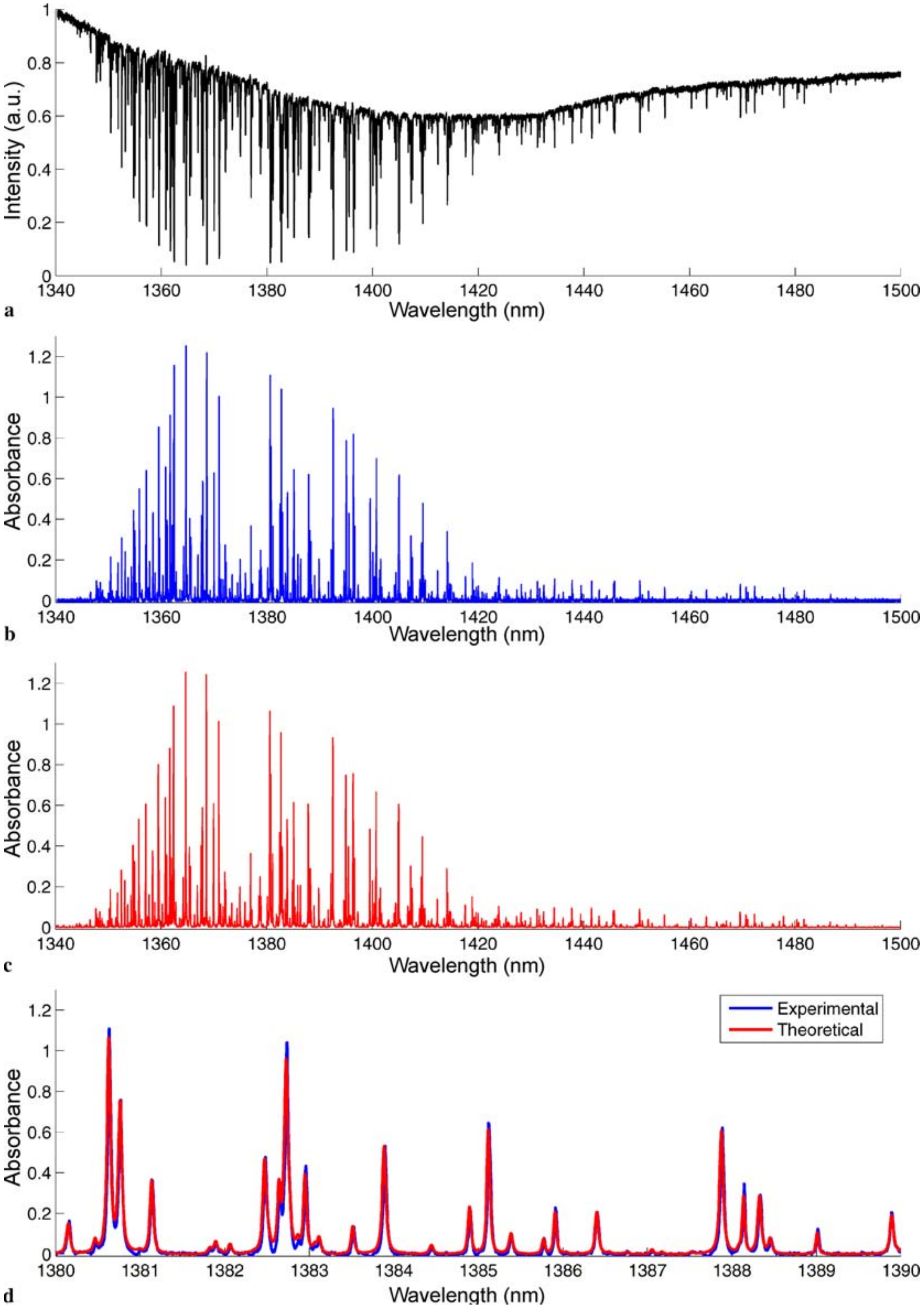

FIGURE 3 (**a**) Intensity of the SC radiation transmitted through air with a relative humidity of 39%. The absorption lines observed correspond to rovibrational overtone transitions of H_2O. (**b**) Corresponding H_2O absorbance spectrum. (**c**) Theoretical spectrum calculated using line parameters from the HiTran database at the experimental conditions. (**d**) Magnified view of the 1380–1390 nm region, showing both experimental and HiTran H_2O peaks [14]

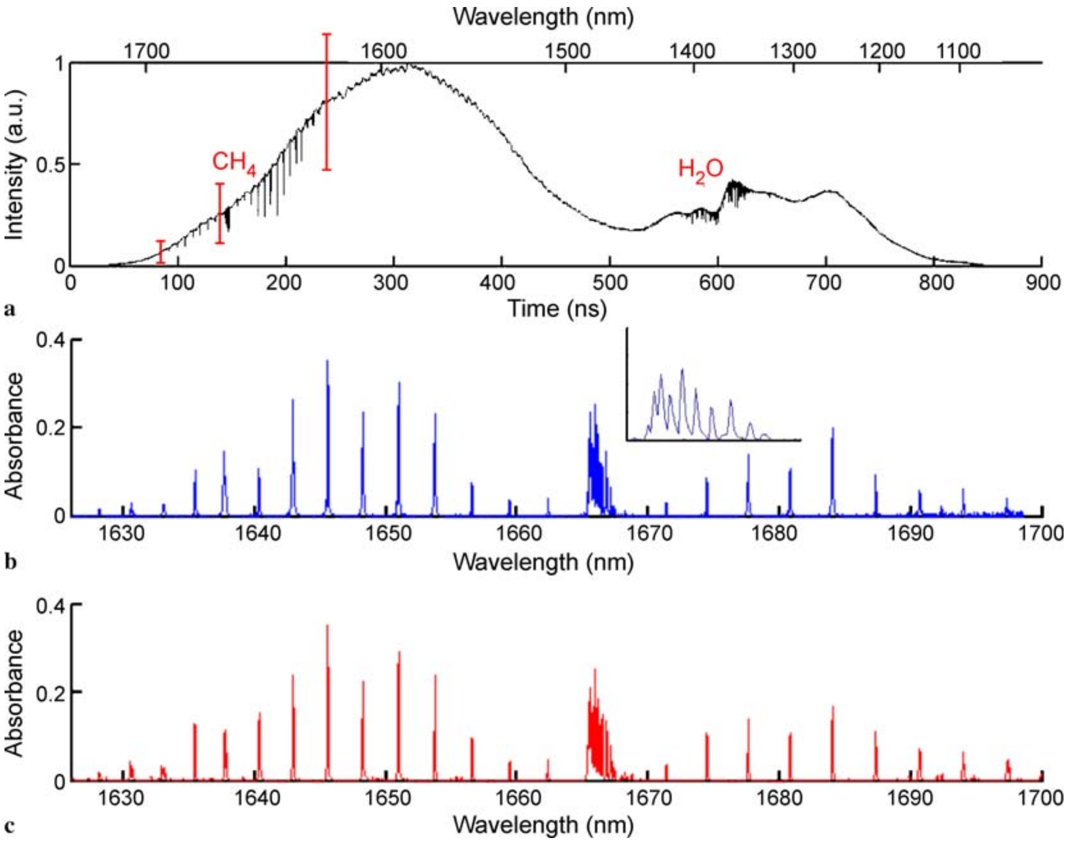

FIGURE 4 (**a**) Intensity of the dispersed supercontinuum pulse, transmitted through a CH_4/air mixture. The standard deviation of the supercontinuum spectral profile is indicated by the *red error bars*. (**b**) Experimental CH_4 absorbance spectrum, corresponding to an average of 1000 wavelength scans, recorded using the oscilloscope. The acquisition time for this 80 nm wide spectrum was 0.9 ms. The *inset* shows the magnified view of the *Q*-branch. (**c**) A theoretical spectrum, based on line parameters for CH_4 obtained from the HiTran database, calculated at the experimental conditions [46]

tion measurement. The agreement between the two is seen to be reasonably good. Fitting a baseline to the transmission trace, to use as the reference spectrum for calculation of the absorbance, works well for spectra containing narrowband absorption features, as in Fig. 4. For broadband absorbers, however, an independent reference measurement of the SC spectral profile is required. As the fluctuations in the spectral profile can be quite large this must be measured in real-time by employing a balanced detection scheme, where part of the beam is split off and bypasses the sample gas. This reference beam can then be detected using either a separate detector or the same detector after being delayed in time through the use of a suitable length of fibre [52].

The temporal resolution of this type of concentration measurement is determined by the repetition rate of the pump laser and by the number of wavelength scans averaged before each concentration measurement datum is calculated. In the present case the maximum repetition rate of the pump laser is restricted to around 1 MHz, in order to avoid overlapping the blue wing of one spectrum with the red wing of the following spectrum. The amount of averaging, however, only depends on the level of precision required. In Fig. 5a five sequentially recorded experimental spectra, corresponding to averages of only 10 wavelength scans, are shown. The total acquisition time for each of those spectra was thus only 9 µs, corresponding to a continuous acquisition rate of 113 kHz. This is sufficiently fast to effectively freeze and resolve almost any turbulent or reactive flow process. In Fig. 5b a time-series of CH_4 column density (molecules/m^2) data determined from the individual spectra is shown. The entire time-series covers just over 1 ms, in which time 120 independent concentration measurements were performed. The time series of CH_4 column densities is seen to be stable, with a relative scatter of only 2.6%, which represents the precision of the measurement, as the gas composition is constant over such short timescales. As the standard deviation, σ, of the baseline in the spectra in Fig. 5a is around 4×10^{-3}, a minimum detectable absorbance (2σ) of around 8×10^{-3} is predicted at a repetition rate of 113 kHz. As the spectral intensity fluctuations are very large, it is crucial that the reference trace used to calculate absorbance is either extracted from the individual measured transmission traces, as is done here, or is measured on a shot-to-shot basis.

5 Microscopy

The excellent spatial coherence and high spectral brightness of SC sources make them ideally suited to replace conventional laser sources in confocal microscopy applications [18]. Traditionally high resolution confocal microscopy is constrained by the number of available excitation lines from conventional laser sources [53]. He-Ne and rare gas ion lasers are the lasers of choice in the overwhelming majority of commercial confocal microscopy instrumentation [54]. Diode lasers are beginning to make an impact at the blue end of the spectrum but a typical confocal microscopy system will feature between 4 and 8 discrete excitation wavelengths, ranging between 410 and 600 nm. This limits access to the full spectral information available from fluorescent specimens. Microscopy systems based around Ti:sapphire laser technology are continuously wavelength tuneable, but restricted to two-photon excitation and have a limited spectral range (typ-

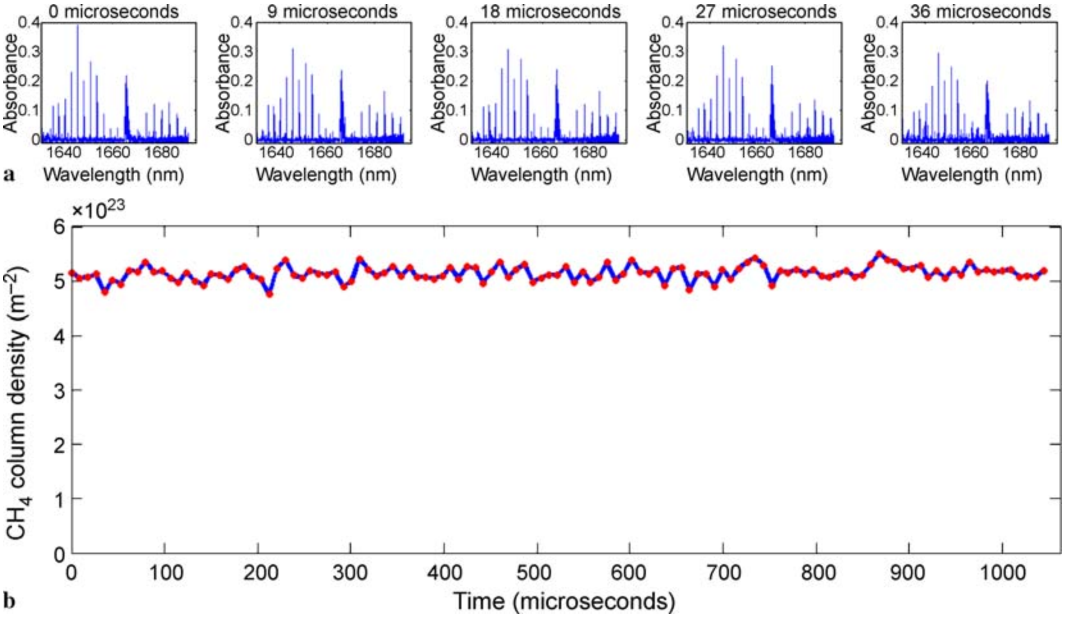

FIGURE 5 (**a**) Sequence of CH_4 absorption spectra, recorded at an acquisition rate of 113 kHz. (**b**) Time series of corresponding measured CH_4 column density [46]

ically 700–1000 nm). In biological applications for example immense advantage would be derived from fully resolved fluorescence excitation and emission scans [55]. This is because fluorescent labels are used to tag individual cellular constituents (e.g. proteins) with high selectivity and specificity, and subtle shifts in the spectral properties of the reporter fluorophores convey information on molecular function. For example the binding of two proteins may be verified via shifts in the spectral characteristics of the reporter fluorophores: As the proteins come into close proximity, electrostatic interactions between the fluorophores increase, resulting in subtle shifts of excitation and emission characteristics as well as in the fluorescence lifetimes [56]. Combinations of fluorophore moieties and excitation and detection methods may thus be used to measure functional changes in molecular systems inside living cells, reporting on such complex phenomena as protein binding, aggregation, and conformational changes. A fully flexible approach giving full spectral information of the system under investigation offers the greatest wealth of information [57].

Such hyperspectral imaging approaches have also great potential for the label-free in vivo diagnosis of diseased tissue. Currently, tissue is mostly analysed ex situ. The methods require patient tissue to be excised via surgical biopsy, followed by time consuming biophysical and chemical preparation protocols before analysis by microscopic methods. Unfortunately, most of the contrast agents used in the laboratory do not meet safety standards for use in humans and therefore lack approval for use in the clinic. The ability to perform diagnostics of diseased tissue without the need for any extrinsic contrast agents would thus provide key advantages for in-clinic applications [58]. Fully wavelength flexible excitation and emission modalities would improve contrast between healthy and diseased tissue with potential for direct, in vivo, applications [59].

Supercontinuum sources are beginning to make an impact in these domains: In confocal microscopy their potential was first demonstrated in 2004 [18]. The short pulse length (femtosecond to picosecond) and high repetition rate (10 s of MHz) characteristic of SC radiation makes them ideal for time-resolved techniques such as TCSPC [17], and even two-photon excitation with SC sources has been demonstrated [60].

In our laboratory, we have developed a fully wavelength flexible confocal microscopy system that permits arbitrary combinations of excitation and emission wavelengths for the analysis of fluorescent samples [19]. We have recently added fluorescence lifetime measurements to this system, which together with the spectrofluorometric capability offers a wealth of information on the sample under investigation

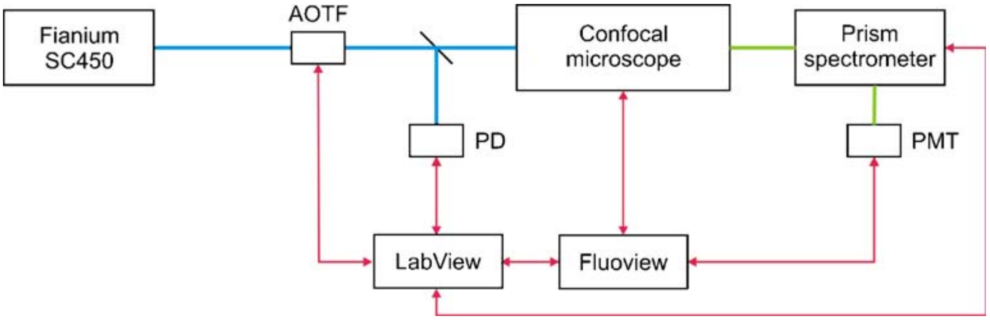

FIGURE 6 Schematic set-up for confocal imaging system (*AOTF* acousto-optic tuneable filter, *PD* photo diode, *PMT* photomultiplier tube)

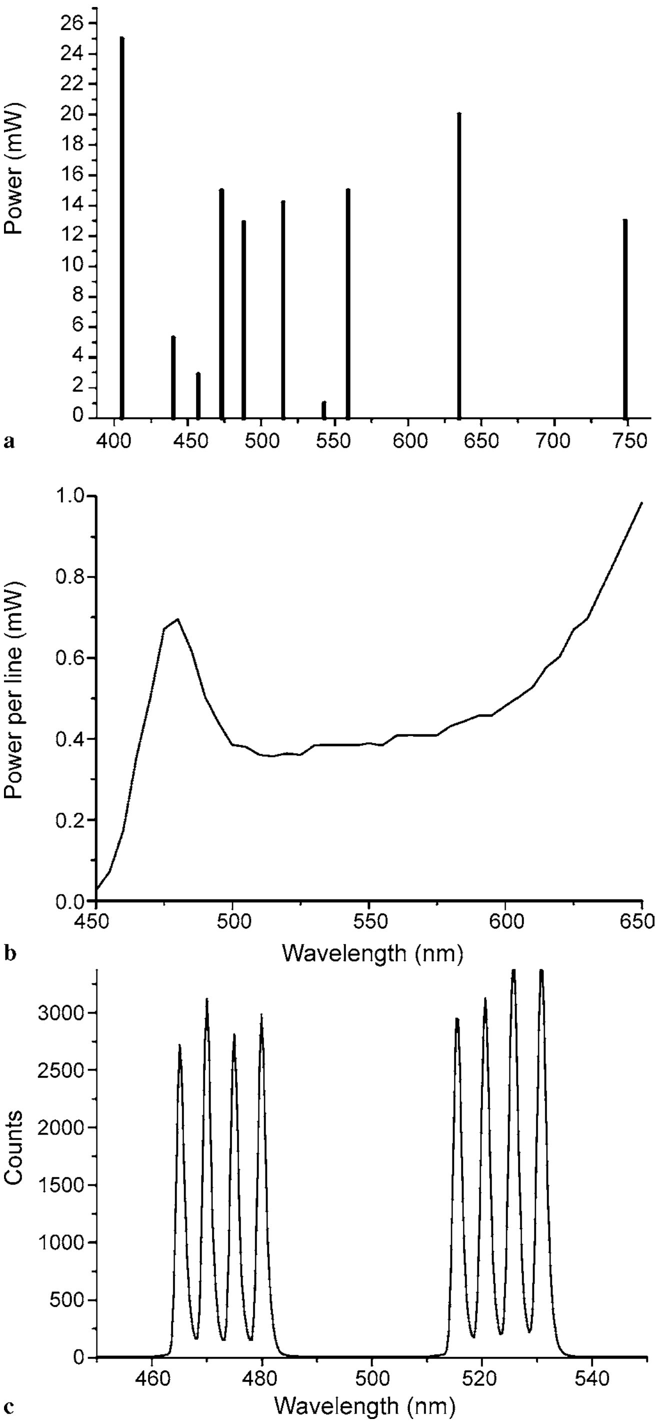

FIGURE 7 (**a**) Available excitation lines for a top of the range commercial confocal microscope platform. (**b**) Output from supercontinuum source used in current setup. The spectrum is clipped at 650 nm but extends all the way to 2000 nm. (**c**) Simultaneous selection of 8 excitation lines with individually adjustable intensity with AOTF excitation filter

and its environment. Figure 6 shows a schematic diagram of the system we have developed. The output from a fibre laser pumped supercontinuum source (Fianium SC450) is filtered with a dichroic mirror to remove infrared frequency components, and the visible portion of the beam is directed through an acousto-optical tunable filter (AOTF, AA Electrooptic) before being directed into the scanner unit of a commercial confocal microscopy platform (Olympus Fluoview FV300). The AOTF and confocal microscope are controlled via software (National Instruments). All original functions of the confocal microscope platform are retained, such as region of interest (ROI) and vector scanning. The configuration permits continuous access to a spectrum spanning from approximately 450 to 700 nm with an available power density of around 1 mW per nm. Up to 8 excitation wavelengths could be controlled simultaneously and independently. Figure 7b shows the available excitation spectrum. Figure 7a shows all available laser lines for a state-of-the-art commercial confocal laser system with multiple fixed-wavelength lasers. The system has an almost flat response of around 10% relative throughput (from fibre exit to objective light output) from 450 to 650 nm and then drops off towards 700 nm. Longer wavelengths up to 2000 nm emitted by the SC could be put to use if suitable optics are substituted. The AOTF and optics inside our confocal scanner drop off markedly in efficiency below 450 and above 650 nm. Multiple excitation wavelengths can be selected simultaneously with the AOTF. As an example of this capability, Fig. 7c displays the spectrum of the beam that is transmitted through the AOTF when 8 lines are switched on simultaneously. The linewidth per excitation wavelength is around 1 nm and is determined by the AOTF transmission characteristics. The fluorescence signal from the sample is collected by a fibre mounted behind the confocal pinhole and imaged into a custom-built, high efficiency prism spectrometer, following design guidelines given in [61]. We have built an electrically controlled slit system, permitting the signal band pass and centre wavelength to be continually adjusted. The AOTF and detector spectrometer combination offer great flexibility for full hyperspectral imaging. Construction details and a full specification of the system have been extensively reported in a previous publication [19]. In this paper images of a thin section of the rhizome of *Convallaria majalis* are presented to demonstrate its capabilities.

To demonstrate the capabilities of the multispectral confocal microscope, we present fluorescence measurements of a thin section of the rhizome of *Convallaria majalis*. The sample is stained with safranin and fast green dyes, but also exhibits autofluorescence. This mix of emission and excitation signatures is ideal for analysis through wavelength-resolved imaging. The sample was imaged using an excitation-emission scan, with excitation wavelengths from 500–640 nm and emission wavelengths from 540–680 nm. The emission wavelength bandpass was 10 nm. The minimum separation between excitation and emission wavelengths was 10 nm to avoid interference from elastic scattering. The fluorescence signals were corrected for variations in the excitation intensity as a function of wavelength. The data was analyzed in three ways. Firstly, the mean excitation wavelength was calculated for every pixel. This was calculated by summing together the fluorescence signal in all emission bandpasses, and then adding these together weighted by the excitation wavelength. The result was normalized by the total fluorescence signal for all excitation and emission wavelengths. This effectively calculates the mean excitation wavelength, and is demonstrated in the equation below:

$$\hat{\lambda}_{\mathrm{ex}} = \sum_{\lambda_{\mathrm{ex}}} \left(\left(\sum_{\lambda_{\mathrm{em}}} I(\lambda_{\mathrm{ex}},\lambda_{\mathrm{em}}) \right) \lambda_{\mathrm{ex}} \right) \Big/ \sum_{\lambda_{\mathrm{ex}}} \sum_{\lambda_{\mathrm{em}}} I(\lambda_{\mathrm{ex}},\lambda_{\mathrm{em}}) . \quad (2)$$

Secondly the mean emission wavelength was calculated for every pixel, in a similar way to that described for the excitation wavelength above. Finally, the intensity of pixels in a selected region were plotted as contour plots as a function of excitation and emission wavelength. Figure 8 shows the mean excitation wavelength and mean emission wavelength images for the *Convallaria* sample. These images show a clear distinction between different regions of the sample, offering greatly

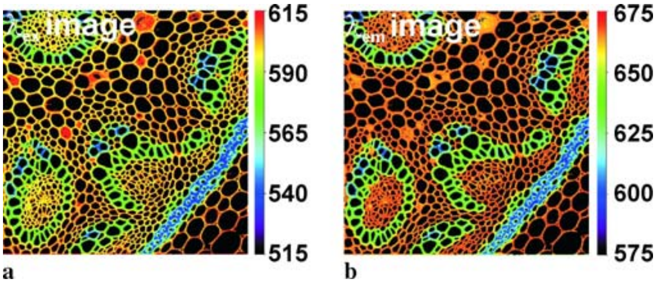

FIGURE 8 Mean excitation (**a**) and emission (**b**) wavelength weighted images from a *Convallaria majalis* sample, processed according to (2). The different structures within the samples are distinguished with high contrast in both images

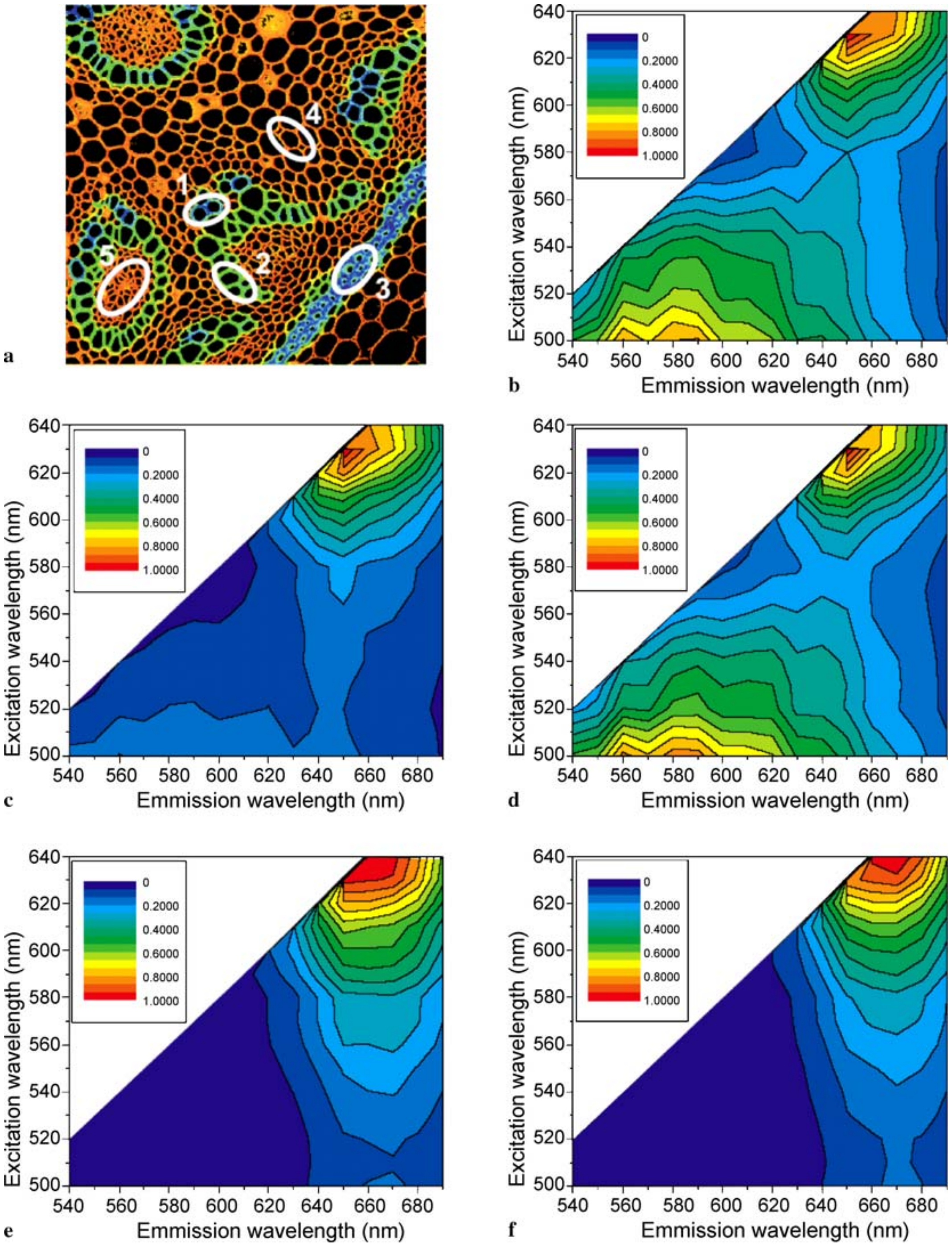

FIGURE 9 (**a**) Mean emission wavelength weighted image highlighting 5 regions for which excitation and emission wavelength contour plots are shown. (**b**–**f**) correspond to regions numbered 1–5, respectively

improved contrast to any conventional imaging mode. Different structures in the sample are very clearly differentiated by subtle variations in autofluorescence and variations in staining efficiency which would be very difficult to see when sampled at discrete excitation wavelengths.

Further examination of the results was performed by looking at excitation-emission contour plots for the five different regions of the sample that are marked in Fig. 9a. The contour plots for regions 1–5 are shown in Fig. 9b–f, respectively. Regions 1 and 2 are different regions of xylem. Region 3 is a section of the endodermis, region 4 is in the pith and region 5 contains phloem. The endodermis and xylem contain lignin, which is stained by the safranin dye. The fast green stains for cellulosic cell walls in the pith and phloem. In the contour plots, three different peaks are evident, corresponding to safranin absorption/emission (500/585 nm), fast green absorption/emission (635/670 nm) and autofluorescence (630/650). The safranin fluorescence is evident in the xylem and endodermis (regions 1–3) as expected. However, from comparison of regions 1 and 2 it is clear that the safranin staining is not even for all xylem. This is shown in Fig. 8a by some xylem (with more safranin) appearing blue, and others (with little safranin) appearing green. The xylem and endodermis all show autofluorescence as well. The phloem and pith (regions 4 and 5) are both stained with fast green, also as expected. In the pith, and to a lesser extent in the phloem, the autofluorescence peak is also evident, although largely merged with the fast green peak. The analysis is very useful as it clearly shows that two peaks are present in the region of 630 nm excitation and 660 nm emission: one which is attributed to fast green and the other to autofluorescence.

A conventional analysis without wavelength resolution would likely not distinguish these two peaks. The image contrast generated between different structures and the identification of autofluorescence shows the great potential of excitation-emission wavelength-resolved fluorescence imaging as an analytical tool. Although image contrast has to be defined in context of the specific application at hand and as thus is difficult to quantify in a generalised way, it is interesting to note the increase in information density in the wavelength-resolved data: For m excitation wavelength steps, with an emission spectrum containing n measurements at different emission wavelengths, the information content increases by a factor m times n. For example for 10 wavelength steps each, each pixel contains 100 spectral datapoints. In our current set-up we are furthermore able to exploit the short pulse length of the excitation radiation such that fluorescence lifetimes can also be measured, providing yet another handle to provide image contrast. For practical applications this opens the door to a range of new possibilities. There is great potential for example, to differentiate healthy and diseased tissue by label-free in vivo detection of autofluorescent signatures. For example cancerous tissue differs biochemically from healthy tissue which may lead to detectable differences in their excitation/emission signatures [62, 63].

6 Conclusions

Broadband supercontinuum-based chemical sensing measurements are attractive in a huge range of applications. The compact sources now available and the delivery of light through solid core fibres with excellent spatial profiles, permits easy incorporation into traditional set-ups and the development of novel diagnostic tools. Emerging pump sources and their miniaturisation (e.g. microchip lasers) will permit ever more integrated devices to be developed in the future. However, there are still technological problems that need to be overcome to make the technology as rugged and reliable as traditional laser technology on the market today: long term stability and reliability issues, intensity fluctuations, and reproducibility are areas where improvements are required (no doubt these will be made, as this very young technology matures). The reproducible manufacture of solid core PCF with predetermined characteristics are also challenges, as well as the tailoring of PCFs towards near UV and mid-IR spectral ranges, which would open up a huge range of opportunities for species sensing.

Many opportunities exist to develop novel applications. In high temperature reactive flows multiple species could be probed in real time. The capability of acquiring spectra covering a large number of H_2O absorption lines also opens up the possibility of measuring temperature distributions [64]. The maximum spectral resolution possible to obtain using the time-of-flight detection scheme described in Sect. 4 is limited by the amount of dispersion that can be employed without introducing too large optical losses. It has recently been shown, though, that this limitation can be lifted using distributed optical amplification in the dispersive fibre unit [65]. The sensitivity of the broadband absorption measurements can be increased by several orders of magnitude by employing cavity-enhanced detection techniques, as previously demonstrated using frequency combs [66] and now also using supercontinuum sources by us [67]. This opens up many new opportunities for trace gas sensing, as part-per-trillion detection limits can be achieved over broad spectral bandwidths. The spectral bandwidths have been limited by spectrometer coverage rather than supercontinuum bandwidths. This is a restriction which in the future could be overcome by employing a Fourier transform spectrometer for detection, which has successfully been demonstrated using frequency comb sources [68]. Up till today, most applications have employed SC radiation in the visible or near-IR spectral regions. New developments in fibre technology and SC generation [31, 41–43] will hopefully extend those possibilities both into the UV and mid-IR regions, where strong electronic and fundamental vibrational transitions can be targeted, thus allowing further increases in detection sensitivity. These developments translate directly into the field of microscopic and life science applications. Probing over extended wavelength ranges and using the short pulse nature to get lifetime information on excited states at increasing acquisition rates, will greatly enhance the diagnostic potential of future optical microscopy. For example an ability to perform diagnostics of diseased tissue without the need for use of any extrinsic contrast agents would provide key advantages for applications in vivo and also for the probing of freshly excised tissue. A whole new range of optical microscopy and endoscopy diagnostic systems can be envisaged, for the characterisation and differentiation of healthy and malignant tissue. Information density and differentiation capabilities could be further improved by combining single-photon, two-photon and lifetime imaging approaches over the entire spectral range from the near-ultraviolet to the near-infrared.

ACKNOWLEDGEMENTS This work was supported by Research Grants from the UK Engineering and Physical Sciences Research Council (EPSRC: EP/C012488/1). J.H. was supported by an Advanced Research Fellowship (EP/C012399/1) from the EPSRC. J.H.F. acknowledges funding from the U.S. Dept. of Energy, Office of Basic Energy Sciences, Division of Chemical Sciences, Geosciences, and Biosciences. C.F.K. would like to thank the Leverhulme Trust for personal sponsorship.

REFERENCES

1 A.R. Alfano (ed.), *The Supercontinuum Laser Source*, 2nd edn. (Springer, Berlin Heidelberg New York, 2006)
2 J.K. Ranka, R.S. Windeler, A.J. Stentz, Opt. Lett. **25**, 25 (2000)
3 J.M. Dudley, G. Genty, S. Coen, Rev. Mod. Phys. **78**, 1135 (2006)
4 T. Udem, R. Holzwarth, T. Hänsch, Nature **416**, 233 (2002)
5 B.J. Schenkel, U. Biegert, U. Keller, C. Vozzi, M. Nisoli, G. Sansone, S. Stagira, S. De Silvestri, O. Svelto, Opt. Lett. **28**, 1987 (2003)
6 K. Mori, K. Sato, H. Takara, T. Ohara, Electron. Lett. **39**, 544 (2003)
7 M.Y. Sfeir, F. Wang, L. Huang, C.-C. Chuang, J. Hone, S.P. O'Brien, T.F. Heinz, L.E. Brus, Science **306**, 1540 (2005)
8 M. Lehtonen, G. Genty, H. Ludvigsen, Appl. Phys. B **83**, 231 (2005)
9 F. Koch, S.V. Chernikov, J.R. Taylor, Opt. Commun. **175**, 209 (2000)
10 J. Hult, R.S. Watt, C.F. Kaminski, J. Lightwave Technol. **25**, 820 (2007)
11 J. Kasparian, M. Rodriguez, G. Méjean, J. Yu, E. Salmon, H. Wille, R. Bourayou, S. Frey, Y.-B. André, A. Mysyrowicz, R. Sauerbrey, J.-P. Wolf, L. Wöste, Science **301**, 61 (2003)
12 P.V. Kelkar, F. Coppinger, A.S. Bhushan, B. Jalali, Electron. Lett. **35**, 1661 (1999)
13 S.T. Sanders, Appl. Phys. B **75**, 799 (2002)
14 R.S. Watt, C.F. Kaminski, J. Hult, Appl. Phys. B **90**, 47 (2008)
15 A.M. Zheltikov, J. Raman Spectrosc. **38**, 1052 (2007)
16 I. Hartl, X.D. Li, C. Chudoba, R.K. Ghanta, T.H. Ko, J.G. Fujimoto, J.K. Ranka, R.S. Windeler, Opt. Lett. **26**, 608 (2001)
17 C. Dunsby, P.M.P. Lanigan, J. McGinty, D.S. Elson, J. Requejo-Isidro, I. Munro, N. Galletly, F. McCann, B. Treanor, B. Onfelt, D.M. Davis, M.A.A. Neil, P.M.W. French, J. Phys. D **37**, 3296 (2004)
18 G. McConnell, Opt. Express **12**, 2844 (2004)
19 J.H. Frank, A.D. Elder, J. Swartling, A.R. Venkitaraman, A.D. Jeyasekharan, C.F. Kaminski, J. Microsc. **227**, 203 (2007)
20 G.P. Agrawal, *Nonlinear Fiber Optics*, 4th edn. (Academic, San Diego, 2007)
21 G. Genty, S. Coen, J.M. Dudley, J. Opt. Soc. Am. B **24**, 1771 (2007)
22 R.H. Stolen, J.P. Gordon, W.J. Tomlinson, H.A. Haus, J. Opt. Soc. Am. B **6**, 1159 (1989)
23 K.J. Blow, D. Wood, IEEE J. Quantum Electron. **QE-25**, 2665 (1989)
24 D. Hollenbeck, C.D. Cantrell, J. Opt. Soc. Am. B **19**, 2886 (2002)
25 J. Hult, J. Lightwave Technol. **25**, 3770 (2007)
26 G. Genty, M. Lehtonen, H. Ludvigsen, J. Broeng, M. Kaivola, Opt. Express **10**, 1083 (2002)
27 J.W. Nicholson, A.K. Abeeluck, C. Headley, M.F. Yan, C.G. Jørgensen, Appl. Phys. B **77**, 211 (2003)
28 G.A. Nowak, J. Kim, M.N. Islam, Appl. Opt. **38**, 7364 (1999)
29 I. Thomann, A. Bartels, K.L. Corwin, N.R. Newbury, L. Hollberg, S.A. Diddams, J.W. Nicholson, M.F. Yan, Opt. Lett. **28**, 1368 (2003)
30 T. Schreiber, J. Limpert, H. Zellmer, A. Tünnermann, K.P. Hansen, Opt. Commun. **228**, 71 (2003)
31 A. Kudlinski, A.K. George, J.C. Knight, J.C. Travers, A.B. Rulkov, S.V. Popov, J.R. Taylor, Opt. Express **14**, 5715 (2005)
32 J.W. Walewski, J.A. Filipa, C.L. Hagen, S.T. Sanders, Appl. Phys. B **83**, 75 (2006)
33 W.J. Wadsworth, N. Joly, J.C. Knight, T.A. Birks, F. Biancalana, P.S.J. Russel, Opt. Express **12**, 299 (2004)
34 B.A. Cumberland, J.C. Travers, S.V. Popov, J.R. Taylor, Opt. Express **16**, 5954 (2008)
35 W.H. Reeves, D.V. Skryabin, F. Biancalana, J.C. Knight, P.S.J. Russell, F.G. Omenetto, A. Efimov, A.J. Taylor, Nature **424**, 511 (2003)
36 P.S.J. Russell, J. Lightwave Technol. **24**, 4729 (2006)
37 J.C. Travers, S.V. Popov, J.R. Taylor, Opt. Lett. **30**, 3132 (2005)
38 C. Lin, R.H. Stolen, Appl. Phys. Lett. **28**, 216 (1976)
39 S.N. Chernikov, Y. Zhu, J.R. Taylor, Opt. Lett. **22**, 5 (1997)
40 C. Lin, V.T. Ngugen, W.G. French, Electron. Lett. **4**, 25 (1978)
41 R.J. Bartula, J.W. Walewski, S.T. Sanders, Appl. Phys. B **84**, 395 (2006)
42 C.L. Hagen, J.W. Walewski, S.T. Sanders, Photon. Technol. Lett. **18**, 91 (2006)
43 C. Xia, M. Kumar, M.-Y. Cheng, R.S. Hegde, M.N. Islam, A. Galvanauskas, H.G. Winful, F.L. Terry, M.J. Freeman, M. Poulain, G. Mazé, Opt. Express **15**, 865 (2007)
44 J.W. Walewski, S.T. Sanders, Appl. Phys. B **79**, 415 (2004)
45 T. Ritari, G. Genty, H. Ludvigsen, Opt. Lett. **30**, 3380 (2005)
46 J. Hult, R.S. Watt, C.F. Kaminski, Opt. Express **15**, 11 385 (2007)
47 L.S. Rothman, D. Jacquemart, A. Barbe, D.C. Benner, M. Birk, L.R. Brown, M.R. Carleer, C. Chackerian Jr., K. Chance, V. Dana, V.M. Devi, J.-M. Flaud, R.R. Gamache, A. Goldman, J.-M. Hartmann, K.W. Jucks, A.G. Maki, J.-Y. Mandin, S.T. Massie, J. Orphal, A. Perrin, C.P. Rinsland, M.A.H. Smith, J. Tennyson, R.N. Tolchenov, R.A. Toth, J. Vander Auwera, P. Varanasi, G. Wagner, J. Quantum Spectrosc. Radiat. Transf. **96**, 139 (2005)
48 W.B. Whitten, Anal. Chem. **54**, 1026 (1982)
49 A.J. Pertzborn, J.W. Walewski, S.T. Sanders, Opt. Commun. **254**, 173 (2005)
50 J. Chou, Y. Han, B. Jalali, IEEE Photon. Technol. Lett. **16**, 1140 (2004)
51 M.T. McCulloch, E.L. Normand, N. Langford, G. Duxbury, D.A. Newnham, J. Opt. Soc. Am. B **20**, 1761 (2003)
52 J.A. Filipa, J.W. Walewski, S.T. Sanders, Appl. Spectrosc. **62**, 230 (2008)
53 R. Borlinghaus, H. Gugel, P. Albertano, V. Seyfried, Proc. SPIE **6090**, 60900T-1 (2006)
54 J.B. Pawley, *Handbook of Biological Confocal Microscopy* (Plenum, New York, 1995)
55 R.A. Schultz, T. Nielsen, J.R. Zavaleta,, R. Ruch, R. Wyatt, H.R. Garner, Cytometry **43**, 239 (2001)
56 J.R. Lakowicz, *Principles of Fluorescence Spectroscopy* (Plenum, New York, 1999)
57 T. Zimmermann, J. Rietdorf, R. Pepperkok, FEBS Lett. **546**, 87 (2003)
58 M. Zellweger, P. Grosjean, D. Goujon, P. Monnier, H. Van Den Bergh, G. Wagnieres, J. Biomed. Opt. **6**, 41 (2001)
59 P.J. Tadrous, J. Siegel, P.M.W. French, S. Shousha, E.N. Lalani, G.W.H. Stamp, J. Pathol. **199**, 309 (2003)
60 J.A. Palero, V.O. Boer, J.C. Vijverberg, H.C. Gerritsen, H. Sterenborg, Opt. Express **13**, 5363 (2005)
61 P. Frederix, M.A.H. Asselbergs, W. Van Sark, D.J. Van Den Heuvel, W. Hamelink, E.L. De Beer, H.C. Gerritsen, Appl. Spectrosc. **55**, 1005 (2001)
62 D.K. Bird, L. Yan, K.M. Vrotsos, K.W. Eliceiri, E.M. Vaughan, P.J. Keely, J.G. White, N. Ramanujam, Cancer Res. **65**, 8766 (2005)
63 P.J. Tadrous, J. Siegel, P.M.W. French, S. Shousha, E.N. Lalani, G.W.H. Stamp, J. Pathol. **199**, 309 (2003)
64 X. Liu, J.B. Jeffries, R.K. Hanson, Am. Inst. Aeronaut. Astronaut. J. **45**, 411 (2007)
65 D.R. Solli, J. Chou, B. Jalali, Nature Photon. **2**, 48 (2008)
66 M.J. Thorpe, K.D. Moll, R.J. Jones, B. Safdi, J. Ye, Science **311**, 1595 (2006)
67 J.M. Langridge, T. Laurila, R.S. Watt, R.L. Jones, C.F. Kaminski, J. Hult, Opt. Express **16**, 10 178 (2008)
68 E. Sorokin, I.T. Sorokina, J. Mandon, G. Guelachvili, N. Picqué, Opt. Express **15**, 16 540 (2007)